

The First Planetary Microlensing Event with Two Microlensed Source Stars

D.P. Bennett^{1,2,M,P}, A. Udalski^{3,O}, C. Han^{4,μ}, I.A. Bond^{5,M}, J.-P. Beaulieu^{6,P}, J. Skowron^{3,O},
B.S. Gaudi^{7,μ}, N. Koshimoto^{1,8,M},
and

F. Abe⁹, Y. Asakura⁹, R.K. Barry¹, A. Bhattacharya^{1,2}, M. Donachie¹⁰, P. Evans¹⁰, A. Fukui¹¹,
Y. Hirao⁸, Y. Itow⁹, M.C.A. Li¹⁰, C.H. Ling⁵, K. Masuda⁹, Y. Matsubara⁹, Y. Muraki⁹,
M. Nagakane⁸, K. Ohnishi¹², H. Oyokawa⁹, C. Ranc¹, N.J. Rattenbury¹⁰, M.K. Rosenthal¹³,
To. Saito¹⁴, A. Sharan¹⁰, D.J. Sullivan¹⁵, T. Sumi⁸, D. Suzuki¹⁶, P.J. Tristram¹⁷, A. Yonehara⁹,

(The MOA Collaboration)

M.K. Szymański³, I. Soszyński³, K. Ulaczyk³, L. Wyrzykowski³,
(The OGLE Collaboration)

D. DePoy¹⁸, A. Gould^{7,19,20}, R. W. Pogge⁷ J.C. Yee,²¹
(The $μ$ FUN Collaboration)

M.D. Albrow²², E. Bachelet²³, V. Batista⁶, R. Bowens-Rubin²⁴, S. Brillant²⁵, J.A.R. Caldwell²⁶,
A. Cole²⁷, C. Coutures⁶, S. Dieters²⁷, D. Dominis Prester²⁸, J. Donatowicz²⁹, P. Fouqué^{30,31},
K. Horne³², M. Hundertmark^{32,33}, N. Kains³⁴, S.R. Kane³⁵, J.-B. Marquette⁶, J. Menzies³⁶,
K.R. Pollard²², C. Ranc¹, K.C. Sahu³⁴, J. Wambsganss³⁷, A. Williams^{38,39}, and M. Zub³⁷

(The PLANET Collaboration)

¹Code 667, NASA Goddard Space Flight Center, Greenbelt, MD 20771, USA;
Email: david.bennett@nasa.gov

²Department of Physics, University of Notre Dame, 225 Nieuwland Science Hall, Notre Dame,
IN 46556, USA;

³Warsaw University Observatory, Al. Ujazdowskie 4, 00-478 Warszawa, Poland

⁴Department of Physics, Chungbuk National University, Cheongju 361-763, Republic of Korea

⁵Institute of Natural and Mathematical Sciences, Massey University, Auckland 0745, New Zealand

⁶Institut d'Astrophysique de Paris, 98 bis bd Arago, 75014 Paris, France

⁷Dept. of Astronomy, Ohio State University, 140 West 18th Avenue, Columbus, OH 43210, USA

⁸Department of Earth and Space Science, Graduate School of Science, Osaka University,
Toyonaka, Osaka 560-0043, Japan

⁸Institute for Space-Earth Environmental Research, Nagoya University, Nagoya 464-8601, Japan

⁹Department of Physics, University of Auckland, Private Bag 92019, Auckland, New Zealand

¹¹Okayama Astrophysical Observatory, National Astronomical Observatory of Japan, 3037-5
Honjo, Kamogata, Asakuchi, Okayama 719-0232, Japan

¹²*Nagano National College of Technology, Nagano 381-8550, Japan*

¹³*Department of Astronomy and Astrophysics, University of California, Santa Cruz, CA 95064, USA*

¹⁴*Tokyo Metropolitan College of Aeronautics, Tokyo 116-8523, Japan*

¹⁵*School of Chemical and Physical Sciences, Victoria University, Wellington, New Zealand*

¹⁶*Institute of Space and Astronautical Science, Japan Aerospace Exploration Agency, Kanagawa 252-5210, Japan*

¹⁷*University of Canterbury Mt. John Observatory, P.O. Box 56, Lake Tekapo 8770, New Zealand*

¹⁸*Department of Physics, Texas A&M University, 4242 TAMU, College Station, TX 77843-4242, USA*

¹⁹*Max-Planck-Institute for Astronomy, Königstuhl 17, 69117 Heidelberg, Germany*

²⁰*Korea Astronomy and Space Science Institute, Daejon 34055, Republic of Korea*

²¹*Harvard-Smithsonian Center for Astrophysics, 60 Garden Street, Cambridge, MA 02138 USA*

²²*University of Canterbury, Dept. of Physics and Astronomy, Private Bag 4800, 8020 Christchurch, New Zealand*

²³*Las Cumbres Observatory Global Telescope Network, 6740 Cortona Drive, suite 102, Goleta, CA 93117, USA*

²⁴*Dept. of Earth, Atmospheric and Planetary Sciences, Massachusetts Institute of Technology, 77 Massachusetts Ave., Cambridge, MA 02139, USA*

²⁵*ESO Vitacura, Alonso de Crdova 3107. Vitacura, Casilla 19001, Santiago 19, Chile*

²⁶*McDonald Observatory, 82 Mt Locke Rd, McDonald Obs TX 79734 USA*

²⁷*School of Math and Physics, University of Tasmania, Private Bag 37, GPO Hobart, 7001 Tasmania, Australia*

²⁸*Department of Physics, University of Rijeka, Radmille Matej vcić 2, 51000 Rijeka, Croatia*

²⁹*Technical University of Vienna, Department of Computing, Wiedner Hauptstrasse 10, 1040 Wien, Austria*

³⁰*CFHT Corporation, 65-1238 Mamalahoa Hwy, Kamuela, Hawaii 96743, USA*

³¹*IRAP, CNRS - Université de Toulouse, 14 av. E. Belin, F-31400 Toulouse, France*

³²*SUPA, School of Physics & Astronomy, University of St Andrews, North Haugh, St Andrews KY16 9SS, UK*

³³*Niels Bohr Institutet, Københavns Universitet, Juliane Maries Vej 30, 2100 København Ø, Denmark*

³⁴*Space Telescope Science Institute, 3700 San Martin Drive, Baltimore, MD 21218, USA*

³⁵*Department of Physics and Astronomy, San Francisco State University, 1600 Holloway Avenue, San Francisco, CA 94132, USA*

³⁶*South African Astronomical Observatory, PO Box 9, Observatory 7935, South Africa*

³⁷*Astronomisches Rechen-Institut, Zentrum für Astronomie der Universität Heidelberg (ZAH), Mönchhofstraße 12-14, 69120 Heidelberg, Germany*

³⁸*Perth Observatory, Walnut Road, Bickley, Perth 6076, Australia*

³⁹*International Centre for Radio Astronomy Research, Curtin University, Bentley, WA 6102, Australia*

^M*MOA Collaboration*

^P*PLANET Collaboration*

^O*OGLE Collaboration*

^μ*μFUN Collaboration*

^R*Robonet Collaboration*

ABSTRACT

We present the analysis of microlensing event MOA-2010-BLG-117, and show that the light curve can only be explained by the gravitational lensing of a binary source star by a star with a Jupiter mass ratio planet. It was necessary to modify standard microlensing modeling methods to find the correct light curve solution for this binary-source, binary-lens event. We are able to measure a strong microlensing parallax signal, which yields the masses of the host star, $M_* = 0.58 \pm 0.10 M_\odot$, and planet $m_p = 0.51 \pm 0.07 M_{\text{Jup}}$ at a projected star-planet separation of $a_\perp = 2.44 \pm 0.26$ AU, corresponding to a semi-major axis of $a = 2.9_{-0.5}^{+1.6}$ AU. Thus, the system resembles a half-scale model of the Sun-Jupiter system with a half-Jupiter mass planet orbiting a half-solar mass star at very roughly half of Jupiter's orbital distance from the Sun. The source stars are slightly evolved, and by requiring them to lie on the same isochrone, we can constrain the source to lie in the near side of the bulge at a distance of $D_S = 6.8 \pm 0.6$ kpc, which

implies a distance to the planetary lens system of $D_L = 3.4 \pm 0.2$ kpc. The ability to model unusual planetary microlensing events, like this one, will be necessary to extract precise statistical information from the planned large exoplanet microlensing surveys, such as the WFIRST microlensing survey.

Subject headings: gravitational lensing: micro, planetary systems

1. Introduction

Gravitational microlensing has a unique niche among planet discovery methods (Bennett 2008; Gaudi 2012) because of its sensitivity to planets with masses extending to below an Earth-mass (Bennett & Rieh 1996) orbiting beyond the snow line (Mao & Paczyński 1991; Gould & Loeb 1992), where planet formation is thought to be the most efficient, according to the leading core accretion theory of planet formation (Lissauer 1993; Pollack et al. 1996). While radial velocity and planetary transit surveys (Wright & Gaudi 2013; Twicken et al. 2016; Ida & Lin 2005; Lecar 2006; Kennedy et al. 2006; Kennedy & Kenyon 2008; Thommes et al. 2008) have found hundreds and thousands of planets, respectively, these methods have much higher sensitivity to planets that orbit very close to their host stars. Their sensitivity to planets like those in our own Solar System is quite limited. Our knowledge of these wide orbit planets extending down to low masses depends on the results of microlensing surveys (Suzuki et al. 2016; Cassan et al. 2012; Gould et al. 2010b). This is the main reason for the selection of the space-based exoplanet microlensing survey (Bennett & Rieh 2002) as a part of the WFIRST mission (Spergel et al. 2015), which was the top-rated large space mission in the 2010 New Worlds, New Horizons decadal survey.

Like the Kepler transit survey (Borucki et al. 2011), the WFIRST exoplanet microlensing survey will primarily be a statistical survey with thousands of expected exoplanet discoveries. However, a large number of planet discoveries does not automatically translate into good statistics if a large fraction of the planet candidates don't allow precise interpretations (Burke et al. 2015; Mullally et al. 2016). Fortunately, the microlensing method predicts a relatively small number of low signal-to-noise planet candidates (Gould et al. 2004) compared to the transit method. Nevertheless, microlensing does have the potential problem of microlensing events that defy interpretation, and these could also add to the statistical uncertainty in the properties of the exoplanet population that can be studied by microlensing.

In the past two years, the analysis of several complicated microlensing events potentially involving planets have been completed. The lens system for OGLE-2007-BLG-349 was revealed to be a circumbinary planet, rather than a 2-planet system with a single host star (Bennett et al. 2016). This removed a significant uncertainty from the Gould et al. (2010b), Cassan et al. (2012) and Suzuki et al. (2016) statistical analyses, which included this event. (If the 2-planet model for OGLE-2007-BLG-349 would have been correct, the 2nd planet would have been the lowest mass ratio planet discovered by microlensing.) Another complicated event was OGLE-2013-BLG-0723,

which was originally claimed to be a planet in a binary star system that was unusually close to the Sun for a microlensing event (Udalski et al. 2015b). This small distance to the lens system was due to a large microlensing parallax signal. However, a more careful analysis of the data (Han et al. 2016) indicated that the light curve was better explained by a binary star system without a planet and a much smaller microlensing parallax signal.

In this paper, we present the analysis of microlensing event MOA-2010-BLG-117, an event that eluded precise interpretation for several years after it was observed and identified as a planetary microlensing event. It has a strong planetary signal, so it must be included in the statistical analysis of MOA data (Suzuki et al. 2016). In fact, the basic character of the light curve was obvious by inspection to many of the authors of this paper. There was a clear planetary signal due to the crossing of two minor image caustics, but detailed models did not provide a good fit. The region between these two minor image caustics is an area of strong demagnification because the minor image is largely destroyed in this region, but the magnification between the MOA-2010-BLG-117 was simply too large. It could only be fit with the addition of a fourth body to increase the magnification between the minor image caustics. This fourth body could be a second source star that would not pass between the minor image caustics and would therefore not suffer the demagnification experienced by the first source. Or the fourth body could be a third lens that could provide additional magnification between the minor image caustics. We found that only triple lens systems with two stars orbited by one planet could come close to fitting the observed light curves. The early modeling could not decide between the binary source and circumbinary planet possibilities.

This paper is organized as follows. In Section 2 we describe the light curve data, photometry and real time modeling that influenced some of the data collection strategy. In Section 3, we describe the systematic light curve modeling of the final data set, which shows that the binary source model must be correct. We also show that we can constrain the distance to the source by requiring that the two source stars have magnitudes and colors that lie on the same isochrone. We describe the photometric calibration and the determination of the primary source star radius in Section 4, and then we derive the lens system properties in Section 5. In Section 6 we consider high angular resolution adaptive optics observations of the MOA-2010-BLG-117 target, and we present a proper motion measurement of the MOA-2010-BLG-117 target that indicates that the source star system lies in the Galactic bulge. Our conclusions are presented in Section 7.

2. Light Curve Data, Photometry and Real Time Modeling

Microlensing event MOA-2010-BLG-117, at RA = 18:07:49.67, DEC = –25:20:40.7, and Galactic coordinates $(l, b) = (5.5875, -2.4680)$, was identified and announced as a microlensing candidate by the Microlensing Observations in Astrophysics (MOA) Collaboration Alert system (Bond et al. 2001) on 7 April 2010. The MOA team subsequently identified the light curve as anomalous at UT 10:19am, 2 August 2010, and this announcement triggered follow-up observa-

tions by the Probing Lensing Anomalies NETwork (PLANET) and the MICROlensing Follow-up Network (μ FUN). The PLANET group observed this event using the 1.0m telescope at the South African Astronomical Observatory (SAAO), and the μ FUN group used the 1.3 SMARTS telescope at the Cerro Tololo Interamerican Observatory (CTIO). The Optical Gravitational Lensing Experiment (OGLE) Collaboration had just updated to their wide field-of-view OGLE-4 system (Udalski et al. 2015a), and their Early Warning System (EWS) was not yet in operation with the new camera (Udalski et al. 1994). So, the OGLE photometry was not produced automatically by the EWS system, but once it became clear that this event had a likely planetary signal, OGLE began to reduce and their circulate their data.

After some systematic trends with airmass were removed from the MOA data and the OGLE data was released, it became clear by inspection that the light curve of this event resembled the case of a source that crossed the region of the triangular minor image caustics, hitting both caustics. This configuration is somewhat similar to those of OGLE-2007-BLG-368 (Sumi et al. 2010) and MOA-2009-BLG-266 (Muraki et al. 2011), except the source for OGLE-2007-BLG-368 only crossed one of the minor image caustics and the source for MOA-2009-BLG-266 was almost as large as the minor image caustics. However, attempts to model this event did not yield good fits with this geometry.

The problem with this minor image caustic crossing model is that the magnification deficit between the two caustic (or cusp) crossings at $t = 5402$ and 5411 is too small. (Note that $t \equiv \text{HJD} - 2450000$). This is evident in Figure 1, which shows the best fit binary lens light curve for MOA-2010-BLG-2010. This light curve has the obvious problem that the magnification between the two caustic/cusp features is higher than the model can accommodate. In fact, the problem is more severe than this figure indicates. In order to minimize this discrepancy between the model and the data, the event is driven to have a very bright source, so that the minor image will be kept at relatively low magnification, which reduces the magnification deficit between the two caustic/cusp features. However, in this case, the source brightness is driven to be $1.5 \times$ brighter than the apparent source star in the OGLE images. This means that negative blending is required, since a negative “blend flux” must be added to the source flux to achieve the relatively faint “star” seen in the unmagnified images. Negative blending is quite possible at low levels due to the variations in the apparent “sky” background due to unresolved stars, but in this case the level of negative blending is too large for such a physical explanation. So, it implies that this model is likely to be incorrect.

Because of these difficulties with the minor image perturbation model and unrelated difficulties with the real-time photometry, early attempts at modeling this event predicted that the relatively bright, well-observed feature at $t \approx 5411$ was the interior of a caustic entrance, where the caustic crossing itself was not observed. But, a subsequent caustic exit never occurred. This made it clear that some version of a planetary minor caustic crossing event was correct, but that an additional lens or source was needed to explain the higher-than-expected brightness between the two caustic/cusp crossings. This possibility was recognized relatively early after the discovery of the light curve anomaly, so we obtained more frequent CTIO V -band observations than usual in the hopes that

they might help reveal a color difference between the two sources of a binary source model.

It was necessary to wait until mid-2011 before the magnification was back at baseline because of the long duration of this microlensing event. After that, the OGLE Collaboration provided optimal centroid photometry using the OGLE difference imaging pipeline (Udalski 2003). Photometry of the MOA data was performed with the MOA pipeline (Bond et al. 2001), which also employs the difference imaging method (Tomaney & Croots 1996). The PLANET collaboration’s SAAO data was reduced with a version of the Pysis difference imaging code (Albrow et al. 2009), and the CTIO data were reduced with DoPHOT (Schechter, Mateo, & Saha 1993). The final data set consists of 4966 MOA observations in the custom MOA-Red passband (roughly equivalent to the sum of Cousins $R+I$), 398 and 48 OGLE observations in the I and V bands, respectively, 150 I -band and 88 V -band observations from the SMARTS telescope in CTIO, 119 I -band observations from SAAO, and 10 K -band observations from the VVV survey (Minniti et al. 2010) using the VISTA telescope at Paranal, which happened to be doing a low cadence survey of the Galactic bulge in 2010.

3. Light Curve Models

Our light curve modeling was done using the image centered ray-shooting method (Bennett & Rhie 1996; Bennett 2010), supplemented with the hexadecapole approximation (Gould 2008; Pejcha & Heyrovsky 2009) that is employed when passes a test for accuracy. For triple lens modeling, we used the code developed for OGLE-2006-BLG-109 (Bennett et al. 2010) and OGLE-2007-BLG-349 (Bennett et al. 2016). Triple lens models have some parameters in common with single and binary lens models. These are the Einstein radius crossing time, t_E , and the time, t_0 , and distance, u_0 , of closest approach between the lens center-of-mass and the source star. For a binary lens, there is also the mass ratio of the secondary to the primary lens, q , the angle between the lens axis and the source trajectory, θ , and the separation between the lens masses, s .

The length parameters, u_0 and s , are normalized by the Einstein radius of this total system mass, $R_E = \sqrt{(4GM/c^2)D_S x(1-x)}$, where $x = D_L/D_S$ and D_L and D_S are the lens and source distances, respectively. (G and c are the Gravitational constant and speed of light, as usual.) For triple lens models, there are an additional separation, mass ratio, and angle to describe the position and mass ratio of the third lens, but we will not explore these models in detail in this paper.

For every passband, there are two parameters to describe the unlensed source brightness and the combined brightness of any unlensed “blend” stars that are superimposed on the source. Such “blend” stars are quite common because microlensing is only seen if the lens-source alignment is $\lesssim \theta_E \sim 1$ mas, while stars are unresolved in ground based images if their separation is $\lesssim 1''$. However, with ground-based seeing, the background contains many unresolved stars, and this makes the background uneven. As a result, it is possible to have realistic cases of “negative blending” if the “negative” brightness of the blend is consistent with the fluctuations in the unresolved stellar

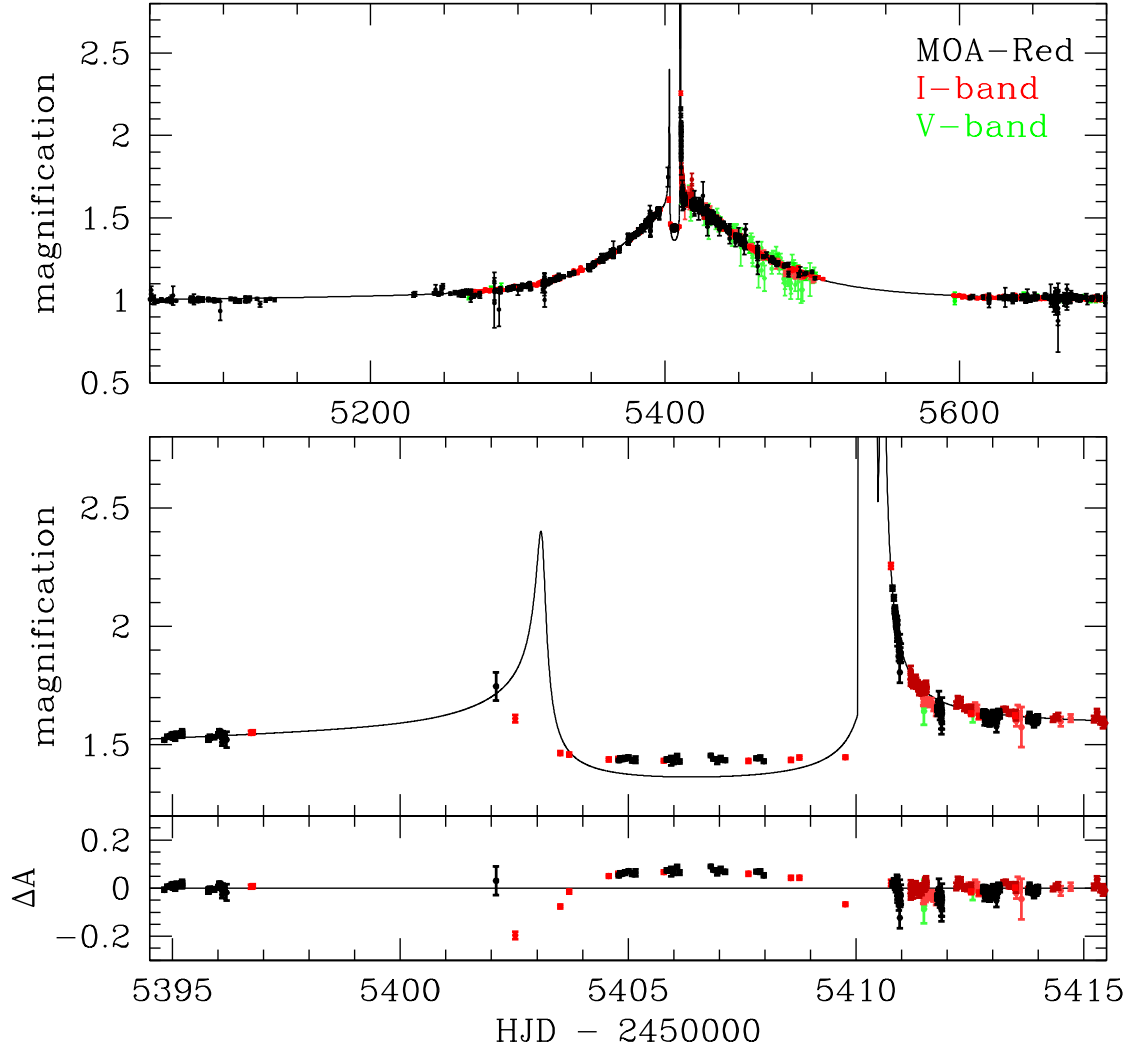


Fig. 1.— The best binary lens model for the MOA-2010-BLG-117 light curve. MOA-Red band data are shown in black. *I*-band data from OGLE, CTIO, and SAAO are shown in red, light red, and dark red, respectively, while the OGLE and CTIO *V*-band data are shown in green and light green.

background. Artificial negative blending can occur with difference imaging photometry that does not attempt to identify a source star in the reference image, but this is just an artifact of the photometry method. In any case, these source and blend fluxes are treated differently from the other parameters because the observed brightness has a linear dependence on them, so for each set of nonlinear parameters, we can find the source and blend fluxes that minimize the χ^2 exactly, using standard linear algebra methods (Rhie et al. 1999).

For the binary source models for MOA-2010-BLG-117, we add a second source to the binary lens model, allowing for a different brightness and color for the second source. The second source has its own t_0 and u_0 values, which we denote as t_{0s2} and u_{0s2} . If the two source stars have exactly the same velocity, then the t_E and θ values for the two sources would also be the same, but due to orbital motion, the t_E and θ values are slightly different. However, the orbital motion of the source stars is much smaller than the orbital motion of the source star system in the Galaxy, so we use parameters to describe the difference of the t_E and θ values. The parameters we use are $dt_{Es2} = t_{Es2} - t_{Es1}$ and $d\theta_{s2} = \theta_{s2} - \theta_{s1}$, where $t_E = t_{Es1}$ and $\theta = \theta_{s1}$.

Our initial attempts to model this event favored the circumbinary models, and the model shown in Figure 2 was the best fit. However, there are several problems with this model. First, although the data are sparse, the model does not provide a good fit to the first cusp approach at $t = 5402$ –5403. However, there is a more serious problem with this model that is demonstrated by Figure 3, which shows how the orbital motion of the binary host stars affects the caustic configuration. The central caustic rotates quite rapidly, such that the angle between the direction of the right-pointing cusp and the source position remains nearly constant throughout the interval between the cusp crossings. This is apparently necessary to avoid having a local light curve peak in the middle of the long minimum at $5403.5 < t < 5410$ at a location where the cusp would be pointing directly at the source. With the rapid orbital motion implied by this model, the source can remain at the same angle with respect to the cusp direction throughout the passage this light curve minimum.

The rapid orbital motion presents a problem, however. The probability of lensing by two stars that aren't bound to each other is quite small ($\sim 10^{-12}$), so we can assume that the two lens stars are bound. If so, then their relative velocity can't be above the escape velocity of the system. As a result, the high relative velocity implies that the lens must be close to the either the lens or the observer, because both of these possibilities allow higher lens orbital velocities when measured in units of Einstein radii per unit time. With the angular source radius, θ_* , derived below in Section 4, we can derive the angular Einstein radius, $\theta_E = \theta_* t_E / t_*$, and this yields the following relation (Bennett 2008; Gaudi 2012)

$$M_L = \frac{c^2}{4G} \theta_E^2 \frac{D_S D_L}{D_S - D_L} = 0.9823 M_\odot \left(\frac{\theta_E}{1 \text{ mas}} \right)^2 \left(\frac{x}{1 - x} \right) \left(\frac{D_S}{8 \text{ kpc}} \right) , \quad (1)$$

where $x = D_L / D_S$. This allows us to determine the lens system mass and convert the measured transverse separation and velocity to physical units at every possible distance for the lens. This exercise tells us that the two stars would be unbound for $0.93 \text{ kpc} < D_L < 7.5 \text{ kpc}$ and $0.05 M_\odot <$

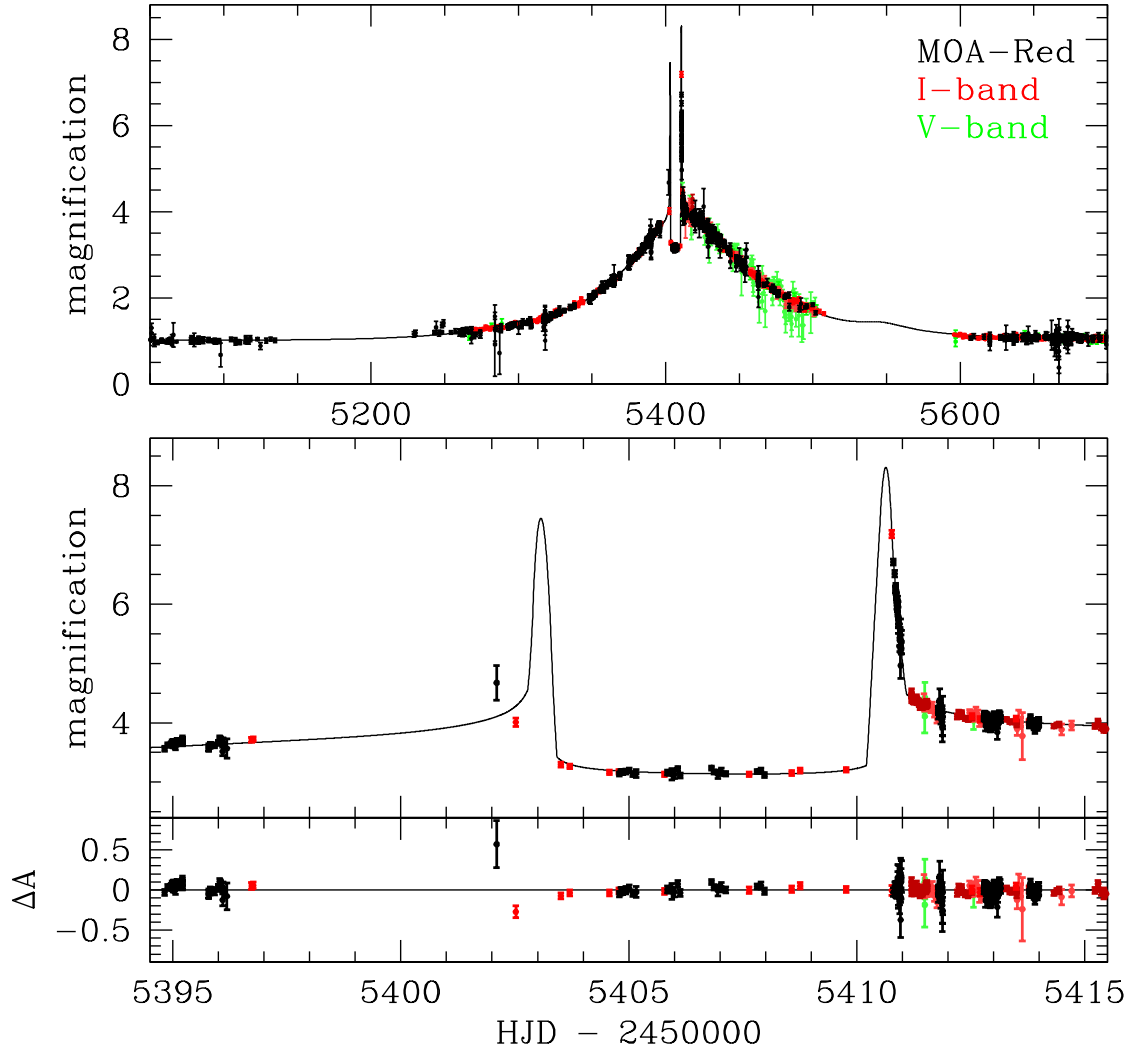


Fig. 2.— The best circumbinary lens model for the MOA-2010-BLG-117 light curve. MOA-Red band data are shown in black. *I*-band data from OGLE, CTIO, and SAAO are shown in red, light red, and dark red, respectively, while the OGLE and CTIO *V*-band data are shown in green and light green.

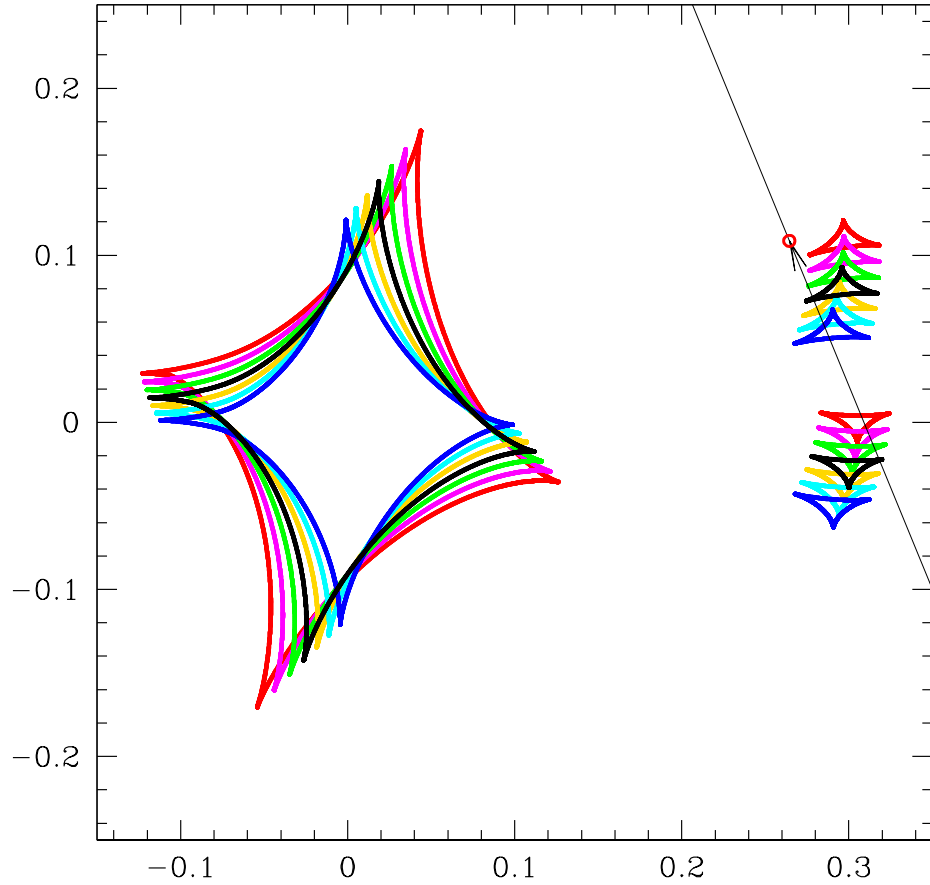


Fig. 3.— The caustic configuration, shown at an interval of two days for the best circumbinary lens model for the MOA-2010-BLG-117 light curve. The caustics are shown at $t = 5401, 5403, 5405, 5407, 5409, 5411$ and 5413 in red, magenta, green, black, gold, cyan, and blue, respectively. The source trajectory is given by the black line with the red circle indicating the source size.

$M_L < 26M_\odot$. However, the microlensing parallax parameters for this model imply a lens system mass of $M_L = 0.218M_\odot$. We can conclude that the lens orbital velocity parameters are too large for a physically reasonable model, so the binary source model is favored.

While the best circumbinary model implied unphysical parameters, in our initial modeling, the best circumbinary model had a better χ^2 than the best binary source models that we found, by $\Delta\chi^2 > 130$. However, the best binary source models from our first round of fitting had an unphysical feature, as well. As with the models with single source, we had been considering the source brightnesses in each passband as independent parameters. But, this allowed the models to move into unphysical regions of parameter space, in which the flux ratio between the two sources was very different for passbands that were nearly identical, like the OGLE, CTIO and SAAO I -bands. In order to avoid these unphysical models, we have modified our modeling code to fix the source flux ratio in the V and I -bands. The flux ratio of source-2 to source-1 is given by f_{s2V} and f_{s2I} in the V and I -bands, respectively. Source-1 is defined to be source that crosses the planetary caustics. For the MOA-red band, we have determined flux ratio parameter $f_{s2Rm} = f_{s2I}^{0.837} f_{s2V}^{0.163}$. This follows from the color transformation that we have derived from the bright stars in this field (Gould et al. 2010a; Bennett et al. 2012),

$$R_{\text{moa}} - I_{\text{O4}} = 0.1630(V_{\text{O4}} - I_{\text{O4}}) + \text{const} , \quad (2)$$

where V_{O4} and I_{O4} refer to the OGLE-IV V -band and I -band magnitudes that have been used for the OGLE light curve data. Note that these restrictions are more more restrictive than those used for some previous non-planetary binary source events that only constrained that data sets using the same passband have the same flux ratio (Hwang et al. 2013; Jung et al. 2017).

With these limitations on the source brightness ratios, we found that the binary source models quickly converged to a solution that was better than the previous best binary source model by $\Delta\chi^2 \sim 200$. It was also better than the best circumbinary model by $\Delta\chi^2 = 68.9$, even though we allowed some of the parameters of the best circumbinary model to take unphysical values.

The best fit light curve model is shown in Figure 4, with the parameters listed in the third column of Table 1. (The best fit solution with $u_0 < 0$ is listed in the fourth column.) Because the sources have different colors, the light curves in the different passbands are different. The green, red, and black curves represent the model light curves in the V , I , and R_{moa} passbands, respectively. The data are plotted with a similar color scheme. We use green and light-green for the OGLE and CTIO V -band data, black for the R_{moa} data, and dark red, red, and light red for the SAAO, OGLE, and μ FUN I -band data, respectively. The caustic configuration for the best fit model is shown in Figure 5. We define the source that crosses the planetary caustic to be source number 1 and the other source to be source 2. Although both sources have similar $|u_0| \sim 0.3$ and $|u_{0s2}| \sim 0.3$ values, we know that only one source comes close to the planetary caustics since we see no evidence of a second encounter of the planetary caustics. This implies that the two sources must pass on different sides of the planetary host star so that the signs of u_0 and u_{0s2} must be different.

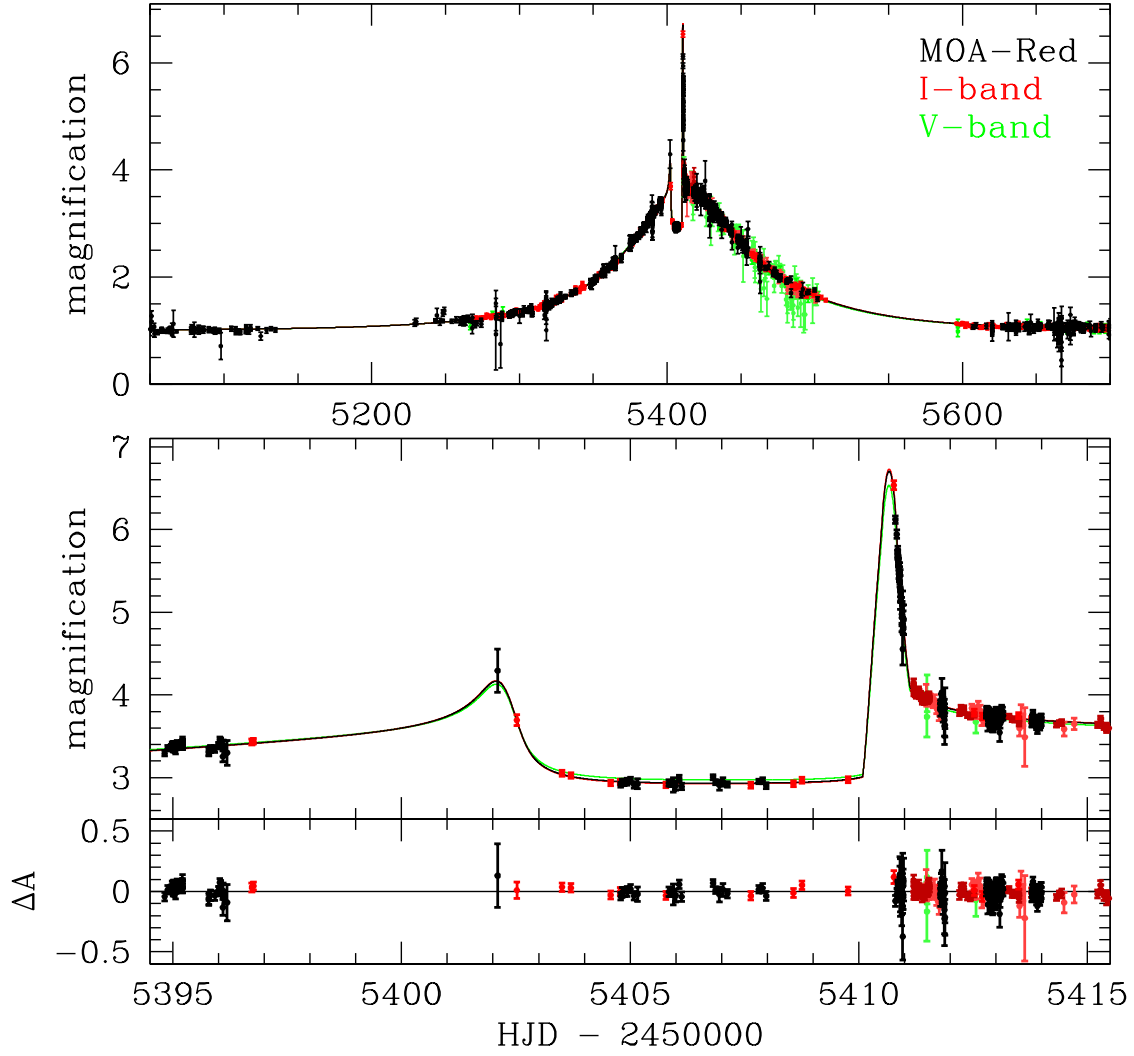


Fig. 4.— The best binary source model for the MOA-2010-BLG-117 light curve. The *I*-band light curves are plotted in different shades of red, with SAAO as dark red, OGLE as red, and CTIO as light red. The OGLE and CTIO *V*-band light curves are plotted in green and light green, respectively. The MOA-red band light curve is plotted in black. The model curves for MOA-red, *I*-band, and *V*-band are plotted in black, red and green, respectively.

Table 1. Best Fit Model Parameters

parameter	units	$t_* > 0.34$ days		$t_* < 0.34$ days	
		$u_0 > 0$	$u_0 < 0$	$u_0 > 0$	$u_0 < 0$
t_E	days	124.86	116.64	124.10	116.36
t_0	$\text{HJD} - 2455400$	19.6267	19.8235	19.7274	19.9430
u_0		0.26765	-0.29109	0.27285	-0.30023
s		0.86465	0.85531	0.86344	0.85180
θ	radians	1.96577	-1.96029	1.94655	-1.95391
q	10^{-3}	0.9797	0.9451	0.7473	0.9279
t_*	days	0.4029	0.3511	0.3154	0.3238
$\pi_{E,N}$		-0.1842	0.1916	-0.1637	0.1599
$\pi_{E,E}$		-0.0199	-0.0394	-0.0167	-0.0278
t_{0s2}	$\text{HJD} - 2455400$	0.2215	0.0228	0.6377	-0.7013
u_{0s2}		-0.28478	0.31192	-0.28366	0.30004
f_{s2I}		0.7517	0.7631	0.7223	0.6700
f_{s2V}		0.8956	0.8364	0.9024	0.8942
dt_{Es2}	days	-11.84	-11.80	-11.47	-10.53
$d\theta_{s2}$	radians	0.28757	-0.23631	0.28995	-0.26236
ω	10^{-3} days $^{-1}$	5.142	-1.401	-1.059	-1.429
\dot{s}	10^{-3} days $^{-1}$	-2.010	-1.607	-1.475	-1.689
$1/T_{\text{Sorb}}$	10^{-3} days $^{-1}$	0.2016	0.2087	0.4535	0.4589
θ_E	mas	0.706	0.781	0.919	0.912
fit χ^2		5745.58	5748.56	7545.84	5749.38

Table 2. MCMC Parameter Distributions

parameter	units	$t_* > 0.34$ days		$t_* < 0.34$ days	
		$u_0 > 0$	$u_0 < 0$	$u_0 > 0$	$u_0 < 0$
t_E	days	123.8(2.0)	118.0(1.4)	125.3(1.7)	117.2(1.1)
t_0	$\text{HJD} - 2455400$	19.60(11)	19.84(6)	19.91(11)	19.91(6)
u_0		0.2688(72)	-0.28882(38)	0.2676(60)	-0.2966(39)
s		0.8642(28)	0.8562(15)	0.8654(23)	0.8533(16)
θ	radians	1.9649(60)	-1.9645(22)	1.9536(63)	-1.9545(20)
q	10^{-3}	0.950(33)	0.998(33)	0.732(24)	0.921(13)
t_*	days	0.387(16)	0.394(21)	0.325(19)	0.320(84)
$\pi_{E,N}$		-0.1854(85)	0.1889(87)	-0.1692(87)	0.1598(95)
$\pi_{E,E}$		-0.0232(33)	-0.0354(25)	-0.0167(57)	-0.0275(29)
t_{0s2}	$\text{HJD} - 2455400$	0.10(12)	0.22(9)	0.47(37)	0.67(8)
u_{0s2}		-0.2869(89)	0.3097(36)	-0.2796(63)	0.2975(39)
f_{s2I}		0.765(66)	0.759(21)	0.745(37)	0.6714(25)
f_{s2V}		0.892(54)	0.911(38)	0.909(30)	0.8897(77)
dt_{Es2}	days	-10.8(4.3)	-13.3(2.2)	-11.56(44)	-8.8(5.3)
$d\theta_{s2}$	radians	0.283(25)	-0.262(15)	0.283(11)	-0.2635(88)
ω	10^{-3} days $^{-1}$	1.67(53)	-2.23(49)	-1.28(51)	-1.32(23)
\dot{s}	10^{-3} days $^{-1}$	-1.99(20)	-1.74(13)	-1.44(13)	-1.708(5)
$1/T_{S\text{orb}}$	10^{-3} days $^{-1}$	0.333(69)	0.235(25)	0.462(55)	0.451(29)
θ_E	mas	0.731(35)	0.724(34)	0.889(51)	0.932(29)
$\mu_{\text{rel,G}}$	mas/yr	2.16(12)	2.24(11)	2.59(16)	2.91(8)
V_{s1}		20.47(3)	20.38(2)	20.50(3)	20.36(2)
I_{s1}		18.01(4)	17.90(2)	18.01(3)	17.85(2)
K_{s1}		14.96(5)	14.85(2)	14.95(4)	14.77(2)
V_{s2}		20.60(4)	20.48(3)	20.60(3)	20.48(2)
I_{s2}		18.30(6)	18.20(2)	18.33(4)	18.28(2)
K_{s2}		15.45(10)	15.37(5)	15.52(6)	15.54(1)
K_{s12}		14.42(2)	14.32(2)	14.44(3)	14.33(2)

The model parameters for the best fit models with $u_0 > 0$ and $u_0 < 0$ are given in Table 1. Table 2 gives the Markov Chain Monte Carlo (MCMC) averages for the models parameters. The source-lens relative velocities for the two sources should be approximately equal because orbital velocity of two stars separated by approximately an Einstein radius in the Galactic bulge is typically about an order of magnitude smaller than the orbital velocity of stars in the inner Galaxy. So, we expect the lens-source relative velocity vectors for the two sources to differ by no more than $\sim 10\%$. However, a $\sim 10\%$ difference between the t_E and θ values for the two sources will have a significant effect on the light curve shape, so we must include parameters to describe t_E and θ for the second source. We chose the parameters $dt_{Es2} \equiv t_{Es2} - t_{Es1}$, where $t_{Es1} \equiv t_E$ and t_{Es2} are the t_E values for the two sources. The different source trajectory angle is described by $d\theta_{s2} \equiv \theta_{s2} - \theta_{s1}$, where $\theta_{s1} \equiv \theta$ and θ_{s2} are the angles between the source trajectories and the lens axis. We also allow for orbital acceleration of the two source stars. We assume a circular orbit for these stars with an orbital period of T_{Sorb} and projected velocities at time $t_{\text{fix}} = 5411$ days implied by the dt_{Es2} and $d\theta_{s2}$ values.

The orbital velocities in the lens system are also important, but since the planetary features in the light curve are detectable for only ~ 10 days, we do not need to include the orbital acceleration of the source. We describe the lens orbital velocities with a rotation of the lens system with angular frequency ω and a velocity of \dot{s} in the separation direction.

This event has a significant orbital microlensing parallax signal (Gould 1992; Alcock et al. 1995), with a χ^2 improvement of $\Delta\chi^2 = 43.93$ with nearly equal contributions from the MOA and

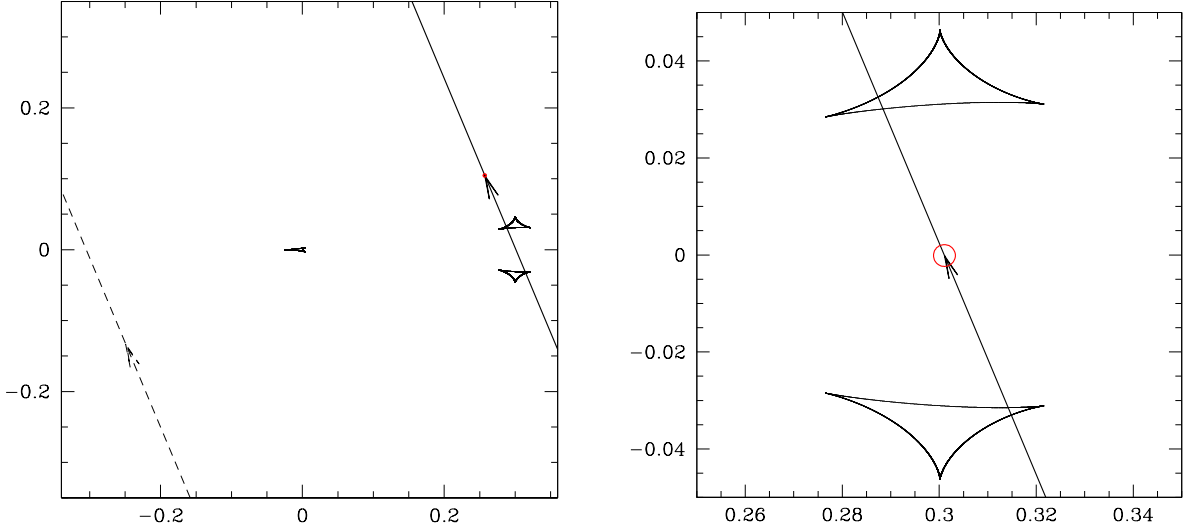


Fig. 5.— The MOA-2010-BLG-117 caustic configuration with the source trajectories shown as the solid and dashed curves for sources 1 and 2, respectively. The arrows give the direction of motion for the sources with respect to the lens system, and the red circle indicates the source of source star 1.

OGLE data sets. The microlensing parallax is defined by a two dimensional vector, π_E with North and East components of $\pi_{E,N}$ and $\pi_{E,E}$ in a geocentric coordinate system moving with the velocity of the Earth measured at time $t_{\text{fix}} = 5411$ days. The parameter t_{fix} is also the reference time for the source and lens positions.

We should note that there are upper limits on the relative velocities between the two sources and between the lens star and planet since they must (almost certainly) be gravitationally bound systems. We assume that the source stars each have a solar mass and compare the 2-dimensional kinetic energy to the maximum binding energy of the source stars (using their separation on the plane of the sky). Then, following Muraki et al. (2011), we apply a constraint on the dt_{Es2} and $d\theta_{s2}$ values. For the lens system, we know the lens mass from the microlensing parallax parameters and the angular Einstein radius, θ_E (Gould 1992; Bennett 2008; Gaudi 2012), and we use this to apply the same constraint. In both cases, the orbital semi-major axis is proportional to θ_E .

These lens and source orbital motion constraints are sensitive to the source radius crossing time through $\theta_E = t_E \theta_*/t_*$, but the light curve constraint on t_* is relatively weak because the caustic crossings are only partially covered. The initial fits to this event with no microlensing parallax, no lens orbital motion, and $dt_{Es2} \equiv 0$ and $d\theta_{s2} \equiv 0$ had a large variation in t_* values ranging from 0.24 days to 0.40 days. When we allowed the dt_{Es2} and $d\theta_{s2}$ values to vary, subject only to the constraint on the maximum orbital motion of the source stars, we found that large values of these parameters were preferred. However, the semi-major axis of the orbit of the source stars is proportional to $\theta_E = t_E \theta_*/t_*$. Thus, a larger t_* implies a smaller θ_E and therefore a smaller semi-major axis. The smaller semi-major axis implies a higher gravitational binding energy, which allows larger lens star velocities implying larger values for dt_{Es2} and $d\theta_{s2}$. Since the data apparently prefer larger values for dt_{Es2} and $d\theta_{s2}$, the constraint on t_* becomes tighter when we include non-zero values of dt_{Es2} and $d\theta_{s2}$ and apply the orbital motion constraint. This can be seen from the t_* values in Tables 1 and 2.

These orbital motion constraints also introduce a set of degenerate solutions with somewhat smaller values of both t_* and π_E . The fifth and sixth columns of Tables 1 and 2 list the parameters for these solutions, which yield systematically higher masses for the host stars. However, the $u_0 > 0$, $t_* < 0.34$ day solution has a smaller planetary mass ratio, so it does not imply a smaller planet mass.

The χ^2 differences between these 4 degenerate solutions are small, as indicated by the bottom row of Table 1. The $u_0 > 0$ solutions are best. The best χ^2 comes from the best fit $u_0 > 0$, $t_* > 0.34$ day solution, but the best $u_0 > 0$, $t_* < 0.34$ day (high mass host) solution is disfavored by only $\Delta\chi^2 = 0.26$. The $\Delta\chi^2$ values for the $u_0 < 0$ solutions are slightly worse with the $u_0 > 0$, $t_* > 0.34$ day (low host mass) solution disfavored by $\Delta\chi^2 = 2.98$ and the corresponding $t_* < 0.34$ day (high host mass) solution disfavored by $\Delta\chi^2 = 3.80$. These small χ^2 differences imply that all of these solutions will contribute to the physical parameter probability distributions, but the $u_0 > 0$ solutions will dominate.

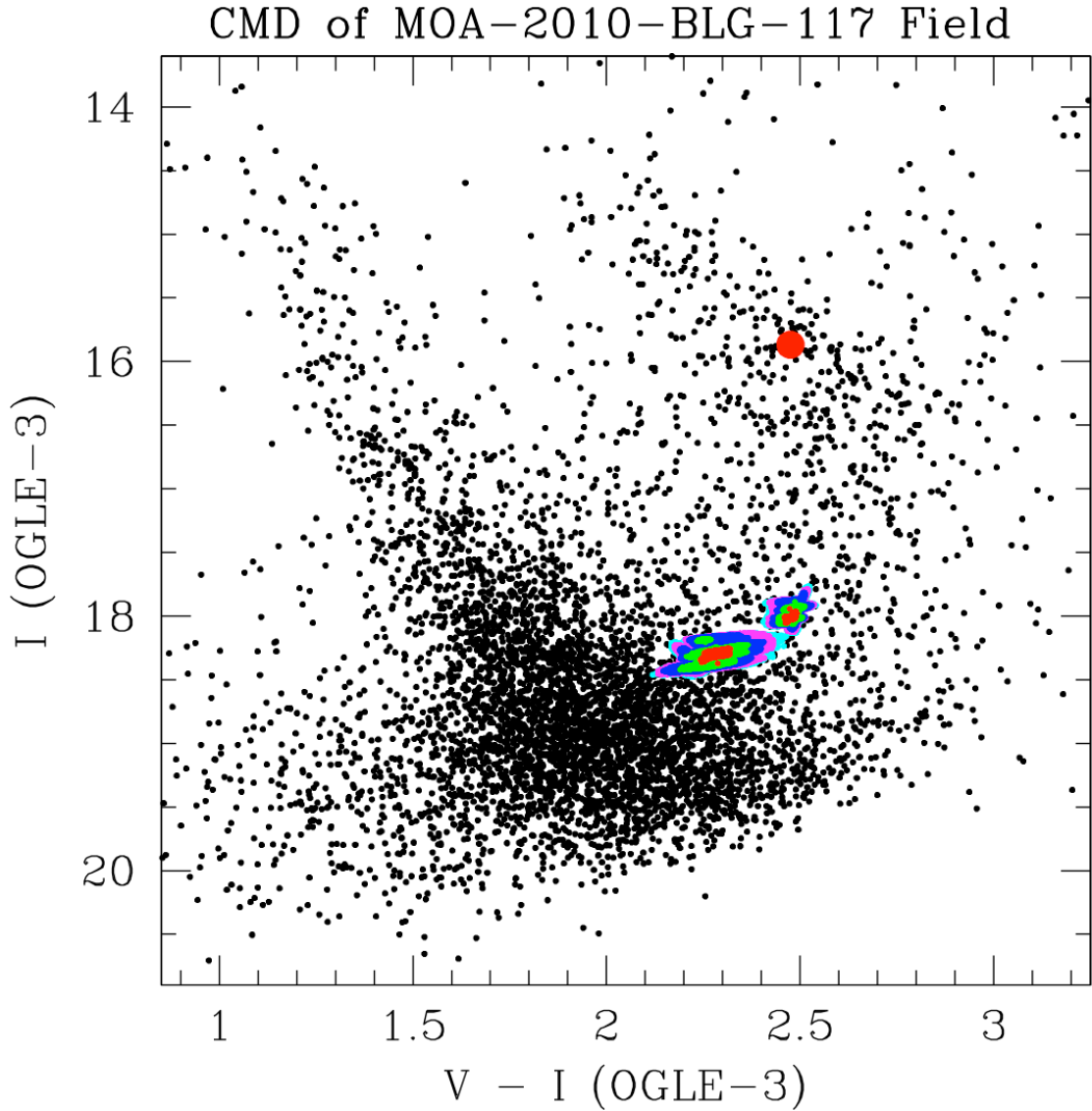


Fig. 6.— The $(V - I, I)$ color magnitude diagram (CMD) of the stars in the OGLE-III catalog (Szymański et al. 2011) within $120''$ of MOA-2010-BLG-117. The red spot indicates red clump giant centroid, and the smaller spots of different colors indicate the magnitude and colors of the two sources from our MCMC calculations. Red, green, blue, magenta, and cyan indicate models that have χ^2 values larger than the best fit model by $\Delta\chi^2 < 1$, $1 < \Delta\chi^2 < 4$, $4 < \Delta\chi^2 < 9$, $9 < \Delta\chi^2 < 16$, and $16 < \Delta\chi^2$, respectively. Source 1 is brighter and redder than source 2.

An unusual feature of this event is that the source system consists of two stars that have both left the main sequence. Contrary to the situation for main sequence stars, the fainter star is bluer than the brighter star as can be seen from Table 2. This is seen even more clearly from the color magnitude diagram shown in Figure 6. This will allow us to constrain the source distance by requiring that the source stars lie on the same isochrone in Section 5.

4. Photometric Calibration and Primary Source Radius

In order to measure the angular Einstein radius, $\theta_E = \theta_* t_E / t_*$, we must determine the angular radius of the source star, θ_* , from the dereddened brightness and color of the source star (Kervella et al. 2004; Boyajian et al. 2014). We determine the calibrated source brightness in the V and I -bands by calibrating the OGLE-IV light curve photometry to the OGLE-III catalog (Szymański et al. 2011). This gives:

$$V_{\text{O3cal}} = 0.2643 + V_{\text{O4}} - 0.0855 (V_{\text{O4}} - I_{\text{O4}}) \quad (3)$$

$$I_{\text{O3cal}} = 0.0403 + I_{\text{O4}} + 0.0032 (V_{\text{O4}} - I_{\text{O4}}) , \quad (4)$$

where V_{O4} and I_{O4} are the OGLE-IV light curve magnitudes and V_{O3cal} and I_{O3cal} are the calibrated OGLE-III magnitudes.

In order to estimate the source radius, we need extinction-corrected magnitudes, and we determine these from the magnitudes and colors of the centroid of the red clump giant feature in the OGLE-III color magnitude diagram (CMD), as indicated in Figure 6. Using the red clump centroid finding method of Bennett et al. (2010), we find the red clump centroid to be located at $I_{\text{O3rc}} = 15.868$ and $V_{\text{O3rc}} - I_{\text{O3rc}} = 2.475$. We compare this to the predicted extinction corrected red clump centroid magnitude and color of $I_{\text{rc0}} = 14.288$ and $V_{\text{rc0}} - I_{\text{rc0}} = 1.06$, which is appropriate (Nataf et al. 2013; Bensby et al. 2013) for the Galactic coordinates of this event, $(l, b) = (5.5875, -2.4680)$. This yields extinction values of $A_I = 1.580$ and $A_V = 2.995$, which implies an extinction corrected primary source magnitude and color of $I_{s1,0} = 16.421$ and $V_{s1,0} - I_{s1,0} = 1.052$ for the best fit model.

These dereddened magnitudes can be used to determine the angular source radius, θ_* . We use the relation from the analysis of Boyajian et al. (2014), but with a restricted range of colors corresponding to $3900 < T_{\text{eff}} < 7000$ (Boyajian, private communication, 2014). We use

$$\log_{10} [2\theta_*/(1\text{mas})] = 0.501414 + 0.419685 (V - I)_{s1,0} - 0.2 I_{s1,0} , \quad (5)$$

and this gives $\theta_* = 2.20 \mu\text{as}$ for the best fit model. As Figure 6 indicates, the uncertainty in the magnitude and color of source 1 is larger than the uncertainty for most events. This is because flux can be traded between the two sources. However, this source radius determination is correlated with the other microlens model parameters, particularly the Einstein radius crossing time, t_E , which occurs in the $\theta_E = \theta_* t_E / t_*$ formula. Therefore, we determine θ_E for each model in our MCMC,

and this yields the θ_E values listed in Table 1: $\theta_E = 0.706 \pm 0.039$ mas for the $u_0 > 0$ solutions and $\theta_E = 0.693 \pm 0.046$ mas for the $u_0 < 0$ solutions.

5. Lens System Properties

When both the angular Einstein radius, θ_E , and the microlensing parallax, π_E , are measured, we can use the following relation (Gould 1992; An et al. 2002; Gould et al. 2004),

$$M_L = \frac{\theta_E c^2 \text{AU}}{4G\pi_E} = \frac{\theta_E}{(8.1439 \text{ mas})\pi_E} M_\odot, \quad (6)$$

to determine the mass of the lens system, but in our case, we have degenerate solutions to consider. The degeneracy allowing different t_* values is probably unique to the specific circumstances of this event. However, the degeneracy between the $u_0 > 0$ and $u_0 < 0$ solutions is a very common degeneracy due to the reflection of the lens plane with respect to the orientation of the Earth’s orbit, which allows us to measure the parallax effect with ground-based data. For high magnification events, the lens-source system has an approximate reflection symmetry, so this $u_0 > 0 \leftrightarrow u_0 < 0$ degeneracy has little effect on $\pi_E \equiv |\pi_E|$. Because the binary source system for MOA-2010-BLG-117 has $u_0 \approx -u_{0,2}$ and source 2 is only ~ 0.3 mag fainter than source 1, the lens and source system in this event also has an approximate symmetry (assuming that the planetary feature has little influence on the microlensing parallax signal). This could be the reason why the distributions of the π_E vector, shown in Figure 7 also show this approximate reflection symmetry. This figure

Table 3. Physical Parameters

Parameter	units	value	2- σ range
D_S	kpc	6.8 ± 0.6	5.6-8.0
D_L	kpc	3.4 ± 0.2	3.0-3.8
M_h	M_\odot	0.58 ± 0.10	0.43-0.76
m_p	M_{Jup}	0.51 ± 0.07	0.42-0.70
a_\perp	AU	2.44 ± 0.26	1.90-2.81
a_{3d}	AU	$2.9^{+1.6}_{-0.5}$	2.1-10.5
V_L	mag	$21.7^{+1.3}_{-1.5}$	19.2-24.1
I_L	mag	$19.8^{+0.9}_{-1.1}$	18.1-21.3
K_L	mag	$18.0^{+0.7}_{-0.9}$	16.8-19.0

Note. — Uncertainties are 1- σ parameter ranges.

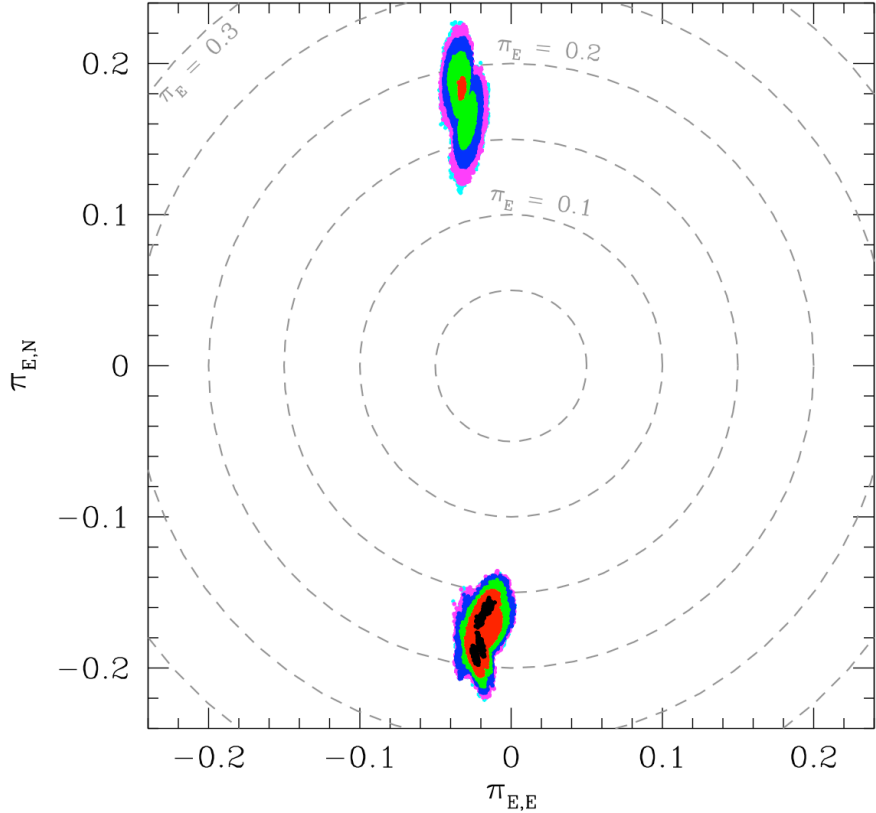


Fig. 7.— The values of the microlensing parallax vector, π_E , from our MCMC runs are shown. The $u_0 > 0$ solutions have $\pi_{E,N} < 0$ and are preferred over the $u_0 < 0$ solutions (with $\pi_{E,N} > 0$) by $\Delta\chi^2 = 9.17$. The MCMC points are color-coded. The points within $\Delta\chi^2 < 1$ are black, and the points within $1 < \Delta\chi^2 < 4$, $4 < \Delta\chi^2 < 9$, $9 < \Delta\chi^2 < 16$, $16 < \Delta\chi^2 < 25$, and $25 < \Delta\chi^2$ are red, green, blue, magenta, and cyan, respectively. The dashed circles indicate curves of constant π_E .

shows the distributions from all four degenerate solutions with best fit parameters listed in Table 1 and Markov chain distributions listed in Table 2. The large and small t_* solutions overlap each other, while the $u_0 > 0$ and $u_0 < 0$ solutions are widely separated with opposite signs for the $\pi_{E,N}$ values. These opposite signs mean that the $|\pi_{E,N}|$ values are very similar for all solutions. The $\pi_{E,E}$ values are also similar and much smaller than $|\pi_{E,N}|$, so the π_E values for all the degenerate solutions are similar. This means that there is overlap in the mass distributions predicted by all four degenerate solutions, but the inclusion of both the low and high t_* solutions has broadened the distribution of predicted host star masses.

As mentioned in Section 3, we impose a requirement that both sources lie on the same isochrone. This requirement is not imposed during the light curve modeling, but it is imposed in our Bayesian analysis that uses all the models from our Markov chains to determine the physical parameters of the lens system. Each light curve model in our Markov chains is weighted by the χ^2 of the best fit of the model source magnitudes and colors to the isochrones. Thus, the location of the source magnitudes and colors in Figure 6 does not depend on these isochrones, but the color coding of the source magnitudes and colors does depend on the fit to the isochrones. We use isochrones from the PAdova and TRieste Stellar Evolution Code (PARSEC) project (Bressan et al. 2012; Chen et al. 2014, 2015; Tang et al. 2014). We find that our modeling results are consistent with isochrones with ages in the range 4–9 Gyr and metalicity in the range $0.28 \leq [\text{Fe}/\text{H}] \leq 0.58$. These values are quite typical of Galactic bulge stars, as indicated by the microlens source stars with high resolution spectra taken at high magnification by Bensby et al. (2013, 2017).

The main practical effect of this isochrone constraint is to force the source star system to be located on the near side of the bulge. The isochrones prefer a source distance of $D_S = 6.2 \pm 1.1$ kpc, but when this priors on the source density and microlensing probability are included, this shifts to $D_S = 6.8 \pm 0.6$ kpc, as given in Table 3.

We determine the physical parameters of this lens system with a Bayesian analysis marginalized over the Galactic model used by Bennett et al. (2014), and the results are summarized in Figures 8 and 9, as well as Table 3. The host star and planet masses (M_h and m_p) are determined directly from equation 6 with the π_E , q , source magnitude and color values determined for each model in our MCMC. The θ_* and θ_E values are determined directly from equations 5, 3 and 4 for each model. The double peaks in the planet and host mass plots are caused by the degenerate solutions with different t_* values. The smaller t_* values imply larger θ_E values through $\theta_E = \theta_* t_E / t_*$, and these solutions also have slightly smaller π_E values. These imply larger lens masses through equation 6. The Galactic model prior has little influence on the lens mass determination because the prior has little variation over the parameter values that are consistent with the MCMC light curve models. The Galactic model has a larger influence on the distance to the lens, because the stellar density has a strong dependence on the distance to the source star, D_S . The relation between the distances to the lens and source stars is given by

$$D_L = \frac{\text{AU}}{\pi_E \theta_E + \pi_S} , \quad (7)$$

where π_S is the parallax of the source star, $\pi_S = \text{AU}/D_S$. As Table 3 indicates, these calculations indicate that the host star has a mass of $M_h = 0.58 \pm 0.10 M_\odot$ and the planet has a mass of $M_p = 0.51 \pm 0.07 M_{\text{Jup}}$, where M_{Jup} is the mass of Jupiter. Assuming a random orientation, their 3-dimensional separation is $a_{3d} = 2.9_{-0.5}^{+1.6}$ AU. The planet mass uncertainty is smaller than the host mass uncertainty because the high host star mass ($t_* < 0.34$ days), $u_0 > 0$ solutions have a lower mass ratio than the other solutions, as indicated in Tables 1 and 2.

The predicted host (and lens) star V , I , and K magnitudes are shown in Figure 9, along with the source distance, D_S . The D_S values are favor a number of discrete distances, as evidenced by the series of peaks in the D_S probability distribution. This is due to our requirement that the two source stars lie on the same isochrone. The isochrone files we used are limited to discrete values of the metalicity, [Fe/H], and log(Age) at intervals of 0.04 and 0.05, respectively. The host star magnitude distributions have double peaks that reflect to the large and small t_* degenerate solutions.

The additional source star also increases our odds of detecting planets orbiting the lens star because the second source provides a second probe of the lens plane. This can be seen in Figure 10, which shows the two cases from our recent exoplanet mass ratio function paper (Suzuki et al. 2016). Over much of the parameter range the second source star approximately doubles the planet detection efficiency. However, this is a much smaller increase than is provided by high magnification

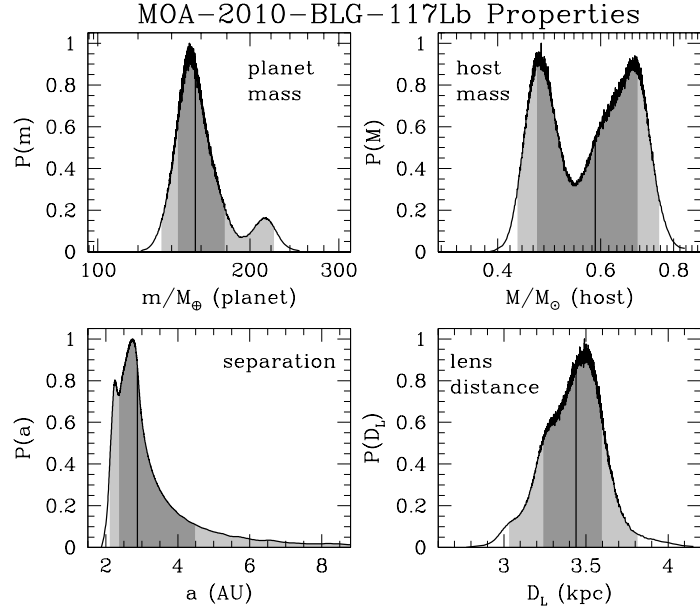


Fig. 8.— Probability distributions of the planet and host star mass, three dimensional separation and lens system distance based on a Bayesian analysis using mass and distance determinations from the MCMC light curve distributions along with prior probabilities from a standard Galactic model.

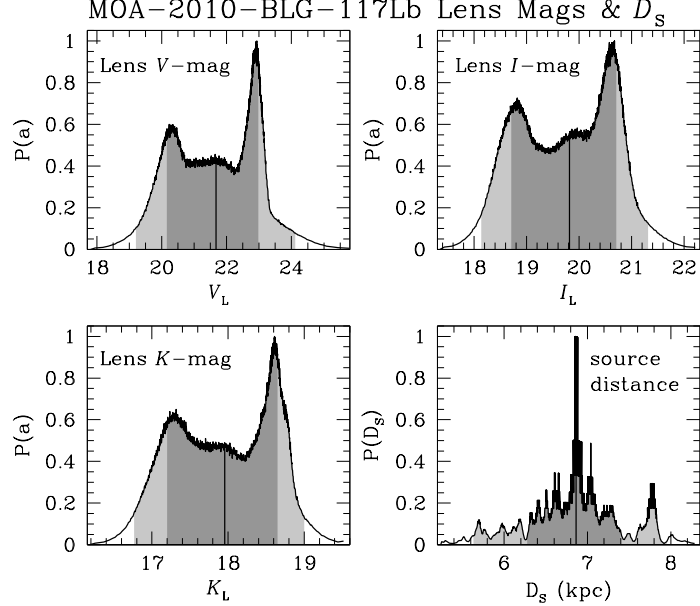


Fig. 9.— Probability distributions of the host star V , I , and I magnitudes, based on our light curve models and Bayesian priors from a standard Galactic model. The multiple peaks of the source distance (D_S) distribution are due to the discrete age and metalicity values used for the isochrone constraints.

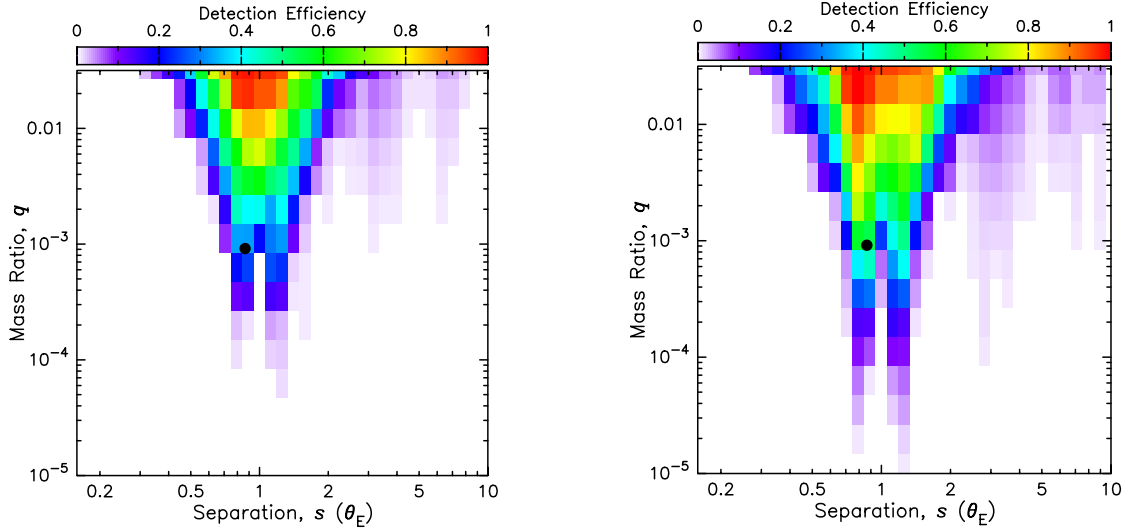


Fig. 10.— Planetary detection efficiency for MOA-2010-BLG-117. The left panel shows the detection efficiency due to the source start that led to the real planet detection, and the right panel shows the planet detection efficiency for the actual event with both source stars. In both cases, the black spots indicate the position of the planet.

events.

6. Keck Follow-up Observations

In an attempt to identify the lens and planetary host star, we have obtained high angular resolution adaptive optics (AO) observations from the Keck 2 telescope. Unfortunately, the seeing conditions were not great compared to some of our other Keck observations (Batista et al. 2015) that achieved a point spread function (PSF) full-width half-max (FWHM) of 60 mas. Our stacked *K*-band image of the MOA-2010-BLG-117 field has a PSF FWHM of 220 mas, and it is shown in Figure 11. The Keck images were taken in 2012, two years after the event. With a lens-source relative proper motion of $\mu_{\text{rel,G}} = 2.14 \pm 0.13$ mas/yr, there is no chance to detect the lens-source

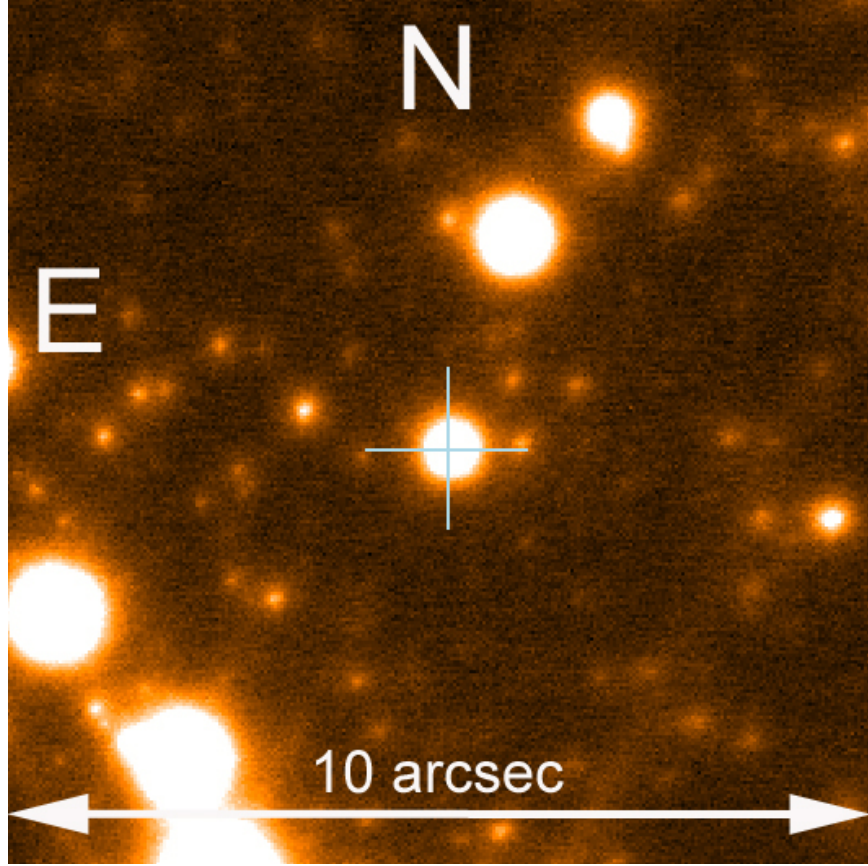


Fig. 11.— The co-added Keck AO image of the target star is indicated by the crosshairs. The target consists of the combined flux of the source stars, the lens (and planetary host star), any bound companions to either the source or lens system, and possibly an unrelated star that happens to be located $\lesssim 0.2''$ from the source.

separation either through image elongation (Bennett et al. 2007, 2015) or a color-dependent image centroid shift (Bennett et al. 2006). However, there is still a chance to detect the unresolved lens star flux on top of the flux from the source stars. In this case, the source stars are relatively bright sub-giants, so it would be difficult to detect a host star as faint as the star indicated by the finite source and microlensing parallax measurements, as discussed in Section 5.

The “star” detected in the Keck AO images is indeed significantly brighter, $K_{\text{Keck}} = 13.97 \pm 0.04$, than the combined flux of the source stars, which is $K_{s12} = 14.42 \pm 0.05$. However, this excess blend flux at $K_b = 15.14 \pm 0.15$ does not match the lens mass and distance derived in Section 5. The predicted host star brightness is $K_L = 18.0^{+0.7}_{-0.9}$, and as can be seen from Figure 9,

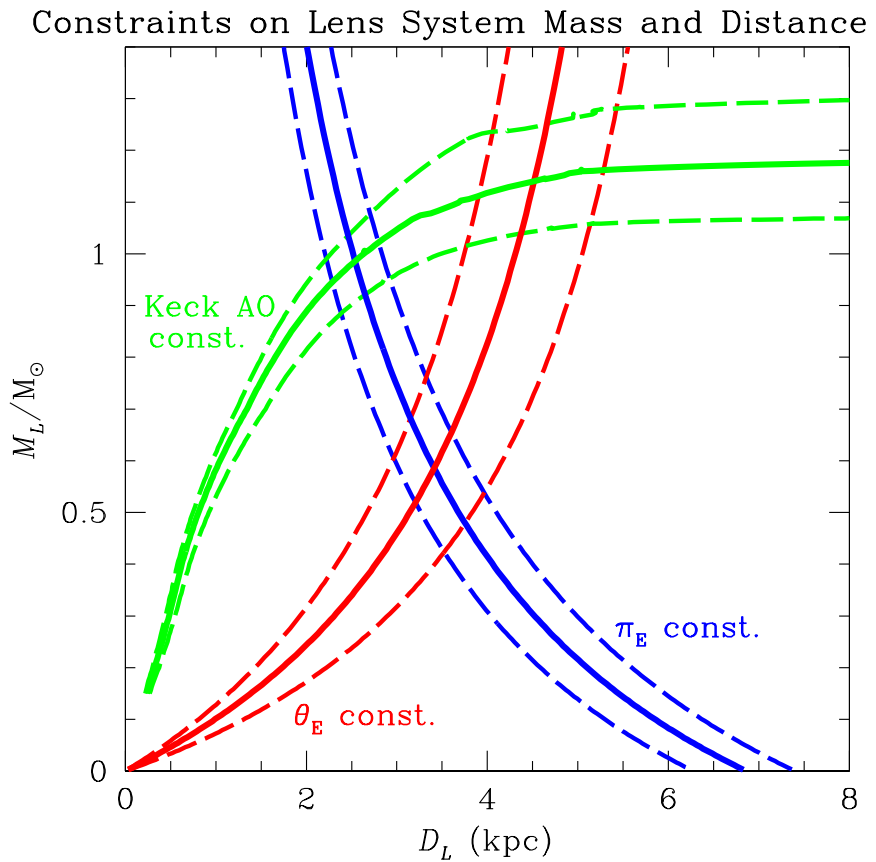


Fig. 12.— Constraints on the host star mass and distance from the microlensing parallax, π_E (in blue), the angular Einstein radius, θ_E (in red), and the host star flux (in green), under the assumption that the excess flux observed in the Keck AO images is due to the host star. The dashed line indicate approximate $1-\sigma$ uncertainty contours (that ignore the correlations between the parameters). For the excess K -band flux, the solid green line is the from a 5 Gyr isochrone and the dashed green lines represent 3 Gyr and 7 Gyr isochrones (Bressan et al. 2012; Chen et al. 2014, 2015; Tang et al. 2014).

the probability of the lens (and host) star being brighter than $K_L < 16$ is negligible. Figure 12 compares the constraints from the microlensing parallax, angular Einstein radius and lens flux constraints, assuming that the excess flux is due to the lens star. Obviously, these constraints are not consistent with each other. The most likely solution to this inconsistency is simply that the excess flux is not due to the lens. The other possibilities that could explain this excess flux at the position of the source star are a binary companion to the lens, a tertiary companion to the source stars, or an unrelated star. A Bayesian analysis using the measured bulge luminosity function and measured frequencies of multiple star systems (Koshimoto et al. in preparation, 2017) gives similar probabilities for each of these possibilities, with slightly larger probabilities for lens and source companions than for an unrelated star.

While we believe that the result from the π_E and θ_E measurements is very likely to be the correct interpretation, we will briefly consider that one of these measurements is wrong. From Figure 12, we see that a host star mass of $M_h \sim 1M_\odot$ at a distance of $D_L \sim 2.6$ kpc would be favored if the blend flux is due to the lens star and the π_E measurement is correct. Alternatively, if the π_E measurement was incorrect, while the θ_E measurement was correct and the blend flux is due to the lens star, then the lens star would have to be an evolved star above a solar mass. The green isochrone curves in Figure 12 are nearly horizontal where they cross the red $\theta_E = \text{const.}$ curve. This is due to the fact that stars evolve very quickly through these evolved phases, and this implies that this solution is particularly unlikely.

A final possibility is that the π_E and θ_E measurements are correct, and the excess flux comes from the planetary host star. This would imply that the assumption made for the red and blue θ_E and π_E curves in Figure 12 that the source is in the Galactic bulge (at $D_S = 6.8 \pm 0.6$ kpc) is not correct. From equation 7, we have $D_S = D_L / (1 - \pi_E \theta_E D_L / \text{AU})$, and this tells us that if the lens system is located at $D_L \approx 0.9$ where the green lens flux curve crosses the $M_h = 0.58 \pm 0.10$ value indicated by the θ_E and π_E measurements (according to equation 6), then the source would be at a distance of $D_S = 1.04$ kpc. This is highly unlikely or at least ruled out for two reasons. First, the rate that stars at this distance are microlensed is more than two orders of magnitude lower than the rate that bulge stars are microlensed. Second, the two source stars appear to reside on the Galactic bulge sub-giant branch of the CMD, shown in Figure 6. Very few foreground disk stars to lie on this portion of the CMD, and there virtually no way to arrange for the fainter star in a binary pair to be bluer than the brighter star.

Another indication that the source stars must reside in the Galactic bulge comes from the proper motion of the source star system. Skowron et al. (2014) has developed a method to determine the proper motion of microlens source stars in the presence of a modest amount of blending with other stars. We have used this method to measured the proper motions of stars brighter than $I < 17.87$, for just over 5 years of OGLE-IV data. (This magnitude cut is two magnitudes below the red clump centroid.) Figure 13 shows that the proper motion of the target, consisting of the two source stars and a blend stars with a magnitude of about the average of the two source stars. If the blend star was the lens, it would be in the Galactic disk, so we would expect that the average

proper motion of the two source stars and the blend to be shifted slightly in the direction of the disk rotation (given by the dashed white line in the NNE direction). Instead, we find that the proper motion of the target to be $(\mu_{E,E}, \mu_{E,N}) = (0.15 \pm 0.34, -0.81 \pm 0.36)$ mas/yr. This clearly indicates that the target is unlikely to be in the disk. Of course, it could be that the blend star and the two source stars are not in the same population, and their proper motions could partially cancel. However, our light curve modeling indicates that the lens-source relative proper motion is in the range 2-3 mas/yr, so if the blend star was the lens, its proper motion could be at most ~ 1 mas/yr in the direction of disk rotation. Thus, it would not have disk kinematics. This tends to confirm our conclusion that the blend star cannot be the lens.

So, we conclude that the source star system resides in the Galactic bulge and that the host star mass and the lens system distance are determined by the π_E and θ_E measurements, as described in Section 5.

7. Discussion and Conclusions

We have presented the first planetary microlensing event with two magnified source stars. This event has an obvious planetary feature, but it could not be modeled with a single source star microlensed by a lens system consisting of one star and one planet. The basic properties of the planetary feature could be explained by models with two source stars or else a circumbinary planet. The choice between these two options was delayed by early difficulties in modeling the event. These difficulties were overcome by adding the requirement that the flux ratio between the two source be consistent with different passbands allows the best light curve model to be found much more easily. The finite source effects and microlensing parallax signal indicate that the planet and host have masses of $m_p = 0.58 \pm 0.10 M_{\text{Jup}}$ and $M_h = 0.51 \pm 0.07 M_{\odot}$ at a two-dimensional separation of $a_{\perp} = 2.44 \pm 0.26$ AU and a distance of $D_L = 3.4 \pm 0.2$ kpc. This is a Jupiter mass-ratio planet orbiting at about twice the distance of the snow line, which is similar to Jupiter's orbit.

One complication in the interpretation of this event is the K -band Keck AO images that indicate an excess of flux at the location of the source. This excess flux is much brighter than the brightness expected from the lens star, based on the mass determined from the θ_E and π_E measurements. We consider possibility that this excess flux could be due to the lens, but we find that the excess flux is more likely to be due to a companion to the lens star, the source stars, or an unrelated star. This is not the first planetary microlensing event with a binary source star, as the planetary event OGLE-2007-BLG-368 (Sumi et al. 2010) has a binary source star that was revealed via the xallarap effect. (Xallarap is the effect of source orbital motion on the microlensing light curve.)

This event was as challenging to model as events with an additional lens mass, either a second star (Gould et al. 2014; Poleski et al. 2014; Bennett et al. 2016) or a second planet (Gaudi et al. 2008; Bennett et al. 2010; Han et al. 2013; Beaulieu et al. 2016). However, events with an

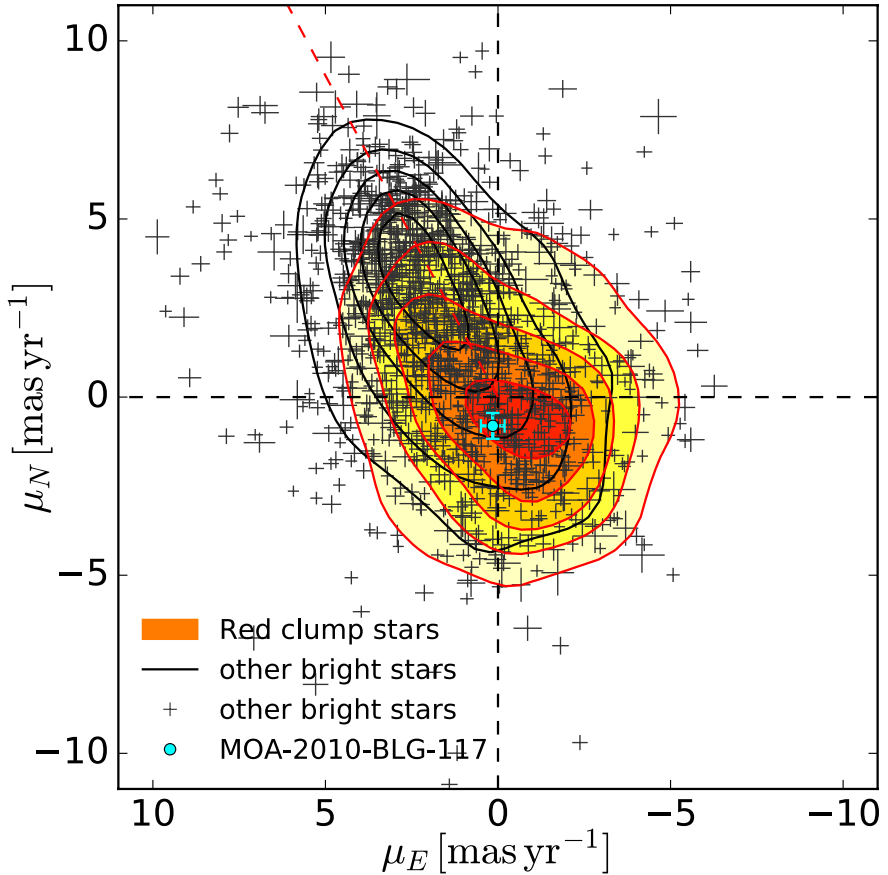


Fig. 13.— The proper motions of stars brighter than the source stars plus blend from the OGLE-IV survey. The red and yellow shaded contours indicate the proper motion distribution of 922 bulge red clump stars and the black contours curves indicate the distribution of the remaining 2239 stars brighter than $I < 17.87$. The dashed red line extending in the NNE direction indicates the direction of Galactic rotation, so we expect the distribution of Galactic disk stars to be extended in the direction of this line. The cyan colored spot with error bars in both the E and N directions indicates the target. The target which consists of the two bound source stars, and a blend star similar in brightness to each of the two source stars. The proper motion of the source stars indicates that they are likely to be bulge stars.

additional lens mass have interesting implications regarding the properties of exoplanet systems, while events with two source stars do not. The only advantage of a second source star is a modest increase in the exoplanet detection efficiency. Nevertheless, microlensing is currently our best method for understanding the population of exoplanets that orbit beyond the snow line, and the statistical analysis of the planet populations probed by the microlensing method requires the correct microlensing model be found for all planetary microlensing events. The new method that we have presented in this paper aids in this effort, and it has enabled the MOA Collaboration analysis that has discovered a break in the exoplanet mass ratio function (Suzuki et al. 2016).

D.P.B., A.B., and D.S. were supported by NASA through grant NASA-NNX12AF54G. This work was partially supported by a NASA Keck PI Data Award, administered by the NASA Exoplanet Science Institute. Data presented herein were obtained at the W. M. Keck Observatory from telescope time allocated to the National Aeronautics and Space Administration through the agency's scientific partnership with the California Institute of Technology and the University of California. The Observatory was made possible by the generous financial support of the W. M. Keck Foundation. The OGLE Team thanks Profs. M. Kubiak and G. Pietrzynski for their contribution to the collection of the OGLE photometric data. The OGLE project has received funding from the National Science Centre, Poland, grant MAESTRO 2014/14/A/ST9/00121 to A.U. Work by C.R. was supported by an appointment to the NASA Postdoctoral Program at the Goddard Space Flight Center, administered by USRA through a contract with NASA. Work by N.K. is supported by JSPS KAKENHI Grant Number JP15J01676. A.G. and B.S.G. were supported by NSF grant AST 110347 and by NASA grant NNX12AB99G. The OGLE project has received funding from the European Research Council under the European Community's Seventh Framework Programme (FP7/2007-2013) / ERC grant agreement no. 246678 to AU.

REFERENCES

Albrow, M. D. et al. 2009, MNRAS, 397, 2099

Alcock, C., Allsman, R. A., Alves, D., et al. 1995, ApJ, 454, L125

An, J. H., Albrow, M. D., Beaulieu, J.-P., et al. 2002, ApJ, 572, 521

Batista, V., Beaulieu, J.-P., Bennett, D.P., et al. 2015, submitted.

Beaulieu, J.-P., Bennett, D. P., Batista, V., et al. 2016, ApJ, 824, 83

Bennett, D.P, 2008, in Exoplanets, Edited by John Mason. Berlin: Springer. ISBN: 978-3-540-74007-0, (arXiv:0902.1761)

Bennett, D.P. 2010, ApJ, 716, 1408

Bennett, D. P., Anderson, J., Bond, I. A., Udalski, A., & Gould, A. 2006, ApJ, 647, L171

Bennett, D.P., Anderson, J., & Gaudi, B.S. 2007, *ApJ*, 660, 781

Bennett, D. P., Batista, V., Bond, I. A., et al. 2014, *ApJ*, 785, 155

Bennett, D. P., Bhattacharya, A., Anderson, J., et al. 2015, *ApJ*, 808, 169

Bennett, D. P., Bond, I. A., Udalski, A., et al. 2008, *ApJ*, 684, 663

Bennett, D. P., Rhie, S. H., Nikolaev, S., et al. 2010, *ApJ*, 713, 837

Bennett, D.P. & Rhie, S.H. 1996, *ApJ*, 472, 660

Bennett, D.P. & Rhie, S.H. 2002, *ApJ*, 574, 985

Bennett, D.P., Rhie, S.H., Udalski, A., et al. 2016, *AJ*, 152, 125

Bennett, D. P., Sumi, T., Bond, I. A., et al. 2012, *ApJ*, 757, 119

Bensby, T., Yee, J. C., Feltzing, S., et al. 2013, *A&A*, 549, A147

Bensby, T., Feltzing, S., Gould, A., et al. 2017, arXiv:1702.02971

Bertelli, G., Girardi, L., Marigo, P., & Nasi, E. 2008, *A&A*, 484, 815

Bond, I. A., Abe, F., Dodd, R. J., et al. 2001, *MNRAS*, 327, 868

Borucki, W. J., Koch, D. G., Basri, G., et al. 2011, *ApJ*, 736, 19

Boyajian, T.S., van Belle, G., & von Braun, K., 2014, *AJ*, 147, 47

Burke, C. J., Christiansen, J. L., Mullally, F., et al. 2015, *ApJ*, 809, 8

Bressan, A., Marigo, P., Girardi, L., et al. 2012, *MNRAS*, 427, 127

Cassan, A., Kubas, D., Beaulieu, J.-P., et al. 2012, *Nature*, 481, 167

Chen, Y., Bressan, A., Girardi, L., et al. 2015, *MNRAS*, 452, 1068

Chen, Y., Girardi, L., Bressan, A., et al. 2014, *MNRAS*, 444, 2525

Gaudi, B. S. 2012, *ARA&A*, 50, 411

Gaudi, B. S., Bennett, D. P., Udalski, A., et al. 2008, *Science*, 319, 927

Gould, A. 1992, *ApJ*, 392, 442

Gould, A. 2008, *ApJ*, 681, 1593

Gould, A., Bennett, D. P., & Alves, D. R. 2004, *ApJ*, 614, 404

Gould, A., Dong, S., Bennett, D. P., et al. 2010a, *ApJ*, 710, 1800

Gould, A., Dong, S., Gaudi, B.S., et al. 2010b, *ApJ*, 720, 1073

Gould, A., Gaudi, B.S., & Han, C., 2004, arXiv:astro-ph/0405217

Gould, A. & Loeb, A. 1992, *ApJ*, 396, 104

Gould, A., Udalski, A., Shin, I.-G., et al. 2014, *Science*, 345, 46

Han, C., Bennett, D.P., Udalski, A., et al., 2016, *ApJ*, 825, 8

Han, C., Udalski, A., Choi, J.-Y., et al. 2013, *ApJ*, 762, L28

Hwang, K.-H., Choi, J.-Y., Bond, I. A., et al. 2013, *ApJ*, 778, 55

Ida, S., & Lin, D.N.C. 2005, *ApJ*, 626, 1045

Jung, Y. K., Udalski, A., Yee, J. C., et al. 2017, *AJ*, 153, 129

Kennedy, G. M., & Kenyon, S. J. 2008, *ApJ*, 673, 502

Kennedy, G.M., Kenyon, S.J., & Bromley, B.C. 2006, *ApJ*650, L139

Kervella, P., Thévenin, F., Di Folco, E., & Ségransan, D. 2004, *A&A*, 426, 297

Lecar, M., Podolak, M., Sasselov, D., & Chiang, E. 2006, *ApJ*, 640, 1115

Lissauer, J.J. 1993, *Ann. Rev. Astron. Ast.*, 31, 129

Mao, S., & Paczyński, B. 1991, *ApJ*, 374, L37

Minniti, D., Lucas, P. W., Emerson, J. P., et al. 2010, *New A*, 15, 433

Mullally, F., Coughlin, J. L., Thompson, S. E., et al. 2016, arXiv:1602.03204

Muraki, Y., Han, C., Bennett, D. P., et al. 2011, *ApJ*, 741, 22

Nataf, D. M., Gould, A., Fouqué, P., et al. 2013, *ApJ*, 769, 88

Pejcha, O., & Heyrovský, D. 2009, *ApJ*, 690, 1772

Poleski, R., Skowron, J., Udalski, A., et al. 2014, *ApJ*, 795, 42

Pollack, J. B., Hubickyj, O., Bodenheimer, P., et al. 1996, *Icarus*, 124, 62

Rhie, S. H., Becker, A. C., Bennett, D. P., et al. 1999, *ApJ*, 522, 1037

Schechter, P. L., Mateo, M., & Saha, A. 1993, *PASP*, 105, 1342

Skowron, J., Udalski, A., Szymański, M. K., et al. 2014, *ApJ*, 785, 156

Spergel, D., Gehrels, N., Baltay, C., et al. 2015, arXiv:1503.03757

Sumi, T., Bennett, D. P., Bond, I. A. et al. 2010, *ApJ*, 710, 1641

Suzuki, D., Bennett, D. P., Sumi, T., et al. 2016, *ApJ*, 833, 145

Szymański, M. K., Udalski, A., Soszyński, I., et al. 2011, *Acta Astron.*, 61, 83

Tang, J., Bressan, A., Rosenfield, P., et al. 2014, *MNRAS*, 445, 4287

Thommes, E.W., Matsumura, S., & Rasio F.A. 2008, *Science*, 321, 814

Tomaney, A.B. & Crotts, A.P.S. 1996, *AJ*112, 2872

Twicken, J. D., Jenkins, J. M., Seader, S. E., et al. 2016, *ApJ*, submitted (arXiv:1604.06140)

Udalski, A. 2003, *Acta Astron.*, 53, 291

Udalski, A., Jung, Y. K., Han, C., et al. 2015b, *ApJ*, 812, 47

Udalski, A., Szymański, M., Kałużny, J., Kubiak, M., Mateo, M., Krzmiński, W., & Paczyński , B. 1994, *Acta Astron.*, 44, 227

Udalski, A., Szymański, M. K., & Szymański, G. 2015a, *Acta Astron.*, 65, 1

Wright, J. T., & Gaudi, B. S. 2013, *Planets, Stars and Stellar Systems. Volume 3: Solar and Stellar Planetary Systems*, 489